




# Wireless, battery-free subdermally implantable photometry systems for chronic recording of neural dynamics

Alex Burton<sup>a,1</sup>, Sofian N. Obaid<sup>b,1</sup>, Abraham Vázquez-Guardado<sup>c</sup>, Matthew B. Schmit<sup>d,e</sup>, Tucker Stuart<sup>a</sup>, Le Cai<sup>a</sup>, Zhiyuan Chen<sup>b</sup>, Irawati Kandela<sup>f</sup>, Chad R. Haney<sup>g</sup>, Emily A. Waters<sup>g</sup>, Haijiang Cai<sup>d,h,i</sup>, John A. Rogers<sup>c,j,k,l,m,n,o,2</sup>, Luyao Lu<sup>b,2</sup> , and Philipp Gutruf<sup>fa,h,i,p,2</sup>

<sup>a</sup>Department of Biomedical Engineering, The University of Arizona, Tucson, AZ 85721; <sup>b</sup>Department of Biomedical Engineering, The George Washington University, Washington, DC 20052; <sup>c</sup>Center for Bio-Integrated Electronics, Northwestern University, Evanston, IL 60208; <sup>d</sup>Department of Neuroscience, The University of Arizona, Tucson, AZ 85721; <sup>e</sup>Graduate Interdisciplinary Program in Neuroscience, The University of Arizona, Tucson, AZ 85721; <sup>f</sup>Developmental Therapeutics Core, Northwestern University, Evanston, IL 60208; <sup>g</sup>Center for Advanced Molecular Imaging, Radiology, and Biomedical Engineering, Northwestern University, Evanston, IL 60208; <sup>h</sup>Bio5 Institute, The University of Arizona, Tucson, AZ 85721; <sup>i</sup>Department of Neurology, The University of Arizona, Tucson, AZ 85721; <sup>j</sup>Feinberg School of Medicine, Northwestern University, Evanston, IL 60208; <sup>k</sup>Department of Electrical Engineering and Computer Science, Northwestern University, Evanston, IL 60208; <sup>l</sup>Department of Neurological Surgery, Northwestern University, Evanston, IL 60208; <sup>m</sup>Department of Chemistry, Northwestern University, Evanston, IL 60208; <sup>n</sup>Department of Mechanical Engineering, Northwestern University, Evanston, IL 60208; <sup>o</sup>Department of Materials Science and Engineering, Northwestern University, Evanston, IL 60208; and <sup>p</sup>Department of Electrical and Computer Engineering, The University of Arizona, Tucson, AZ 85721

Contributed by John A. Rogers, December 19, 2019 (sent for review November 20, 2019; reviewed by Guosong Hong and Jia Liu)

**Recording cell-specific neuronal activity while monitoring behaviors of freely moving subjects can provide some of the most significant insights into brain function. Current means for monitoring calcium dynamics in genetically targeted populations of neurons rely on delivery of light and recording of fluorescent signals through optical fibers that can reduce subject mobility, induce motion artifacts, and limit experimental paradigms to isolated subjects in open, two-dimensional (2D) spaces. Wireless alternatives eliminate constraints associated with optical fibers, but their use of head stages with batteries adds bulk and weight that can affect behaviors, with limited operational lifetimes. The systems introduced here avoid drawbacks of both types of technologies, by combining highly miniaturized electronics and energy harvesters with injectable photometric modules in a class of fully wireless, battery-free photometer that is fully implantable subdermally to allow for the interrogation of neural dynamics in freely behaving subjects, without limitations set by fiber optic tethers or operational lifetimes constrained by traditional power supplies. The unique capabilities of these systems, their compatibility with magnetic resonant imaging and computed tomography and the ability to manufacture them with techniques in widespread use for consumer electronics, suggest a potential for broad adoption in neuroscience research.**

photometry | neural dynamics | wireless | genetically encoded calcium indicator | battery-free

**D**eciphering functional neural connections across the central nervous system is critically important in efforts to discover the underlying working principles, an overarching goal in modern neuroscience. Advanced tools that can record cell-specific signals with high spatiotemporal fidelity in freely behaving subjects are essential to research in this field of study. Current methods for recording such signals rely on genetically encoded calcium indicators (GECIs) capable of targeting cells with high specificity (1–3). Fluorescent signatures from these indicators follow calcium transients associated with cell activity. Practical execution of this experimental approach currently uses telecommunication-grade optical fibers that deliver optical stimuli to genetically targeted cells and relay spectrally separated fluorescence emission to external detection electronics for filtering and digitalization. Such photometric systems can reveal, for example, neurological pathways associated with aggression, movements, and social interactions in behaving animals (4–6). The fiber optic tether represents, however, a key drawback that restricts mobility (7), thereby

constraining experimental paradigms to those that do not require three-dimensional (3D) arenas or studies of multiple subjects in pairs or social groups. The tether can also induce motion artifacts that limit signal fidelity and induce micromotions detrimental to the neuronal interface via formation of glial scarring (8, 9). Recent work on wireless photometers avoid these drawbacks, but these systems rely on head stages with mounted batteries whose bulk and weight cause unwanted effects on behaviors in small animal models and set limits on operating lifetimes (10). An ideal alternative would involve an ultraminiaturized, lightweight, fully subdermal implant, with capabilities for interrogating neural dynamics and device lifetimes that exceed those of the test subjects themselves.

## Significance

**Monitoring neuronal activity with cell specificity in freely behaving animal models can yield insights into underpinning operating mechanisms of the brain. Dynamics of genetically targeted neuronal populations can be recorded through calcium indicators; however, current tools for such measurements are only available with tethers or large and heavy externalized head stages, with potential to influence behaviors of the test subjects and to limit experimental paradigms to simple two-dimensional arenas. Here, we introduce highly miniaturized, wireless, battery-free, and subdermally implantable photometry systems that bypass these limitations to enable chronic recording of neural dynamics in ethologically relevant environments with no impact on test subject behavior. This technology has potential for broad utility in neuroscience research and can enable fundamentally new experiments in neuronal dynamics and simultaneous behavior studies.**

Author contributions: A.B., S.N.O., I.K., J.A.R., L.L., and P.G. designed research; A.B., S.N.O., A.V.-G., M.B.S., T.S., L.C., Z.C., I.K., C.R.H., E.A.W., and H.C. performed research; A.B., S.N.O., A.V.-G., M.B.S., T.S., L.C., Z.C., C.R.H., E.A.W., H.C., J.A.R., L.L., and P.G. analyzed data; and A.B., S.N.O., A.V.-G., J.A.R., L.L., and P.G. wrote the paper.

Reviewers: G.H., Stanford University; and J.L., Harvard University.

Competing interest statement: J.A.R. and J.L. are coauthors on a 2018 review article.

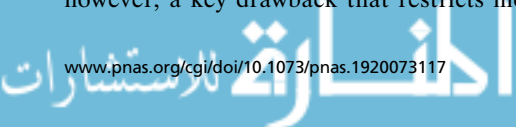
Published under the [PNAS license](#).

<sup>1</sup>A.B. and S.N.O. contributed equally to this work.

<sup>2</sup>To whom correspondence may be addressed. Email: jrogers@northwestern.edu, luyao@gwu.edu, or pgutruf@email.arizona.edu.

This article contains supporting information online at <https://www.pnas.org/lookup/suppl/doi:10.1073/pnas.1920073117/-DCSupplemental>.

First published January 23, 2020.



Here, we present such a system, in the form of a photometric device that couples compact electronics with strategies for wireless power delivery and data transmission, capable of use in some of the smallest animal models, including young mice. Compared to previous work, the devices reported here eliminate the use of batteries and tethers, thereby allowing for continuous and chronic recording of neural activities, in a platform whose small size and weight enable fully subcutaneous implantation. This technology relies critically on strategies for wireless energy harvesting with efficiencies that exceed those of previous work by several times (11, 12). The use of off-the-shelf components facilitates scalable production, with a nonmagnetic construction that allows compatibility with magnetic resonance imaging (MRI) and micro-computed tomography ( $\mu$ CT) imaging, for advanced structural and functional analysis.

## Results

**Miniaturized Wireless Photometry Design.** Fig. 1A displays a layered rendering of the miniaturized implant, designed for recording GECIs dynamics in freely moving subjects using an injectable photometry probe with colocated microscale inorganic light-emitting diode ( $\mu$ -ILED) and photodetector ( $\mu$ -IPD) for fluorescent stimulation and recording, respectively, both interfaced to a microcontroller ( $\mu$ C). A modulated infrared (IR) LED provides the basis for wireless data communication to a separate photodetector via transmission through the skin and fur of the animal. The system receives power wirelessly by magnetic resonant coupling (13.56 MHz) between a primary antenna that encircles the experimental arena and a millimeter-scale receiving antenna on the implant. Constituent layers include a thin dual-sided flexible circuit board composed of rolled annealed copper layers separated by a polyimide film, structured using a high-resolution laser ablation system (LPKF U4). The thin construction leads to a level of mechanical flexibility that allows conformal contact with the curved surface skull and minimizes tissue

damage during surgical implantation (12–14). Each electronic component features a small footprint, with high-performance, low-power operation. All components, listed in *SI Appendix, Fig. S1*, are commercially available, to enable functional reproducibility and alignment with capabilities in scaled manufacturing. The design features an injectable component with a serpentine interconnect geometry to facilitate articulations of the probe during positioning to target a brain region of interest (10).

The operating principles, schematically shown in Fig. 1B, can be supported by electronic components that consume an area of only 0.21 cm<sup>2</sup>, a reduction by 3.5-fold in comparison to previously published examples (11, 12), as shown in detail in *SI Appendix, Fig. S1*. The circuit enables excitation of fluorescence by a  $\mu$ -ILED and amplified detection of this fluorescence by a  $\mu$ -IPD, signal digitalization, and wireless transmission. All of these operations rely on power wirelessly received through coupling to a primary antenna that encloses the experimental arena and connects to a radiofrequency (RF) amplifier (NeuroLux) operating at 13.56 MHz (11). The harvested power is rectified and regulated by a low-dropout voltage regulator (LDO) (3.3 V). The stabilized voltage powers a  $\mu$ C that controls the  $\mu$ -ILED for excitation of fluorescence from the GECIs and a transimpedance amplifier circuit for amplification of photocurrent signals from the  $\mu$ -IPD. Both optical components mount on the tip end of a thin, flexible injectable probe. Amplified signals are subsequently digitalized by a 10-bit analog-to-digital-converter (ADC) integrated in the  $\mu$ C and oversampled at 12-bit precision with four averages and then transmitted using an IR LED (950 nm) with a modulated carrier frequency of 57 kHz and ON/OFF keying with data rates of up to 27 Hz and an radiosity of 0.542 mW/mm<sup>2</sup>. Passage of this light through the scalp attenuates the light by an amount that depends on the species and phenotype, and can range from 53% transmission in albino CD1 IGS mice (12) to 30% for Swiss Webster (albino) species with white fur to as low as ~1% for C57BL/6 mice with black fur (*SI Appendix, Fig. S24*),

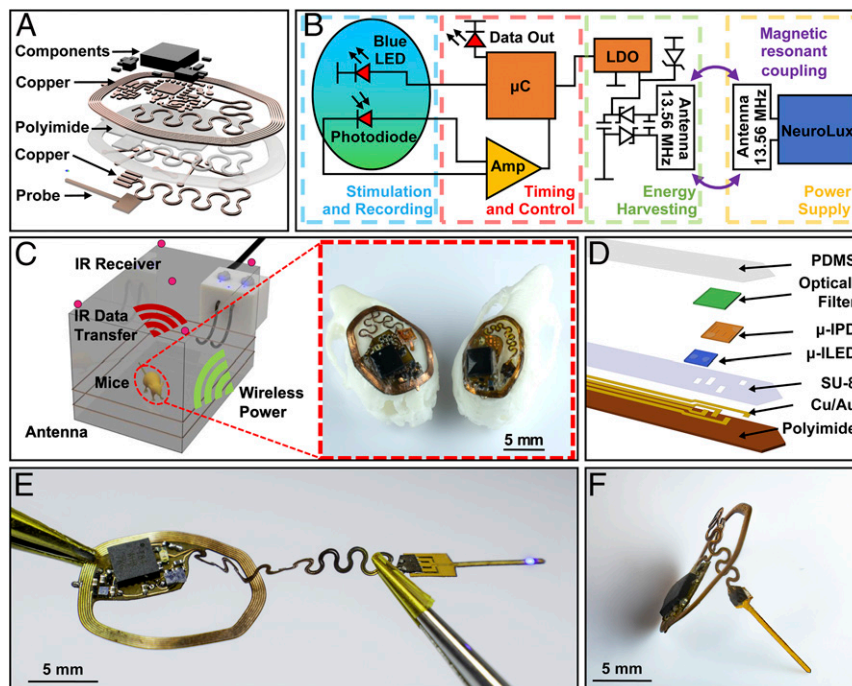


**Fig. 1.** (A) Exploded-view schematic illustration of the photometry device. (B) Block diagram of the circuit function. (C) Rendered 3D schematic illustration of power delivery and data uplink for freely behaving mouse animal models. *Inset* shows implantation of both small (*Right*) and large (*Left*) devices on models of mouse skulls. (D) Schematic exploded-view illustration of a wireless, injectable photometry probe. (E) Photograph of a probe as it is powered in a configuration stretched from its original shape. (F) Side-view photograph of the device.

resulting in a radiosity of  $8.67 \mu\text{W}/\text{mm}^2$ . Attenuation of the IR light predominantly occurs in the fur. Removing the fur by shaving leads to transmission values of  $\sim 70$  to  $80\%$  in all species and subjects examined (SI Appendix, Fig. S2B).

The IR receivers (TSDP34156; Vishay Semiconductors) are highly integrated devices in small packages ( $5.6 \times 6 \times 7 \text{ mm}$ ) that include a lens system, an optical filter ( $900$  to  $1,025 \text{ nm}$ ), an automatic gain control, a bandpass filter that reduces noise at frequencies other than the carrier frequency, and demodulator circuits that pass only the digital data signal to an external  $\mu\text{C}$ . The lower detection threshold is  $0.00015 \mu\text{W}/\text{mm}^2$  even for background ambient irradiances of over  $1 \mu\text{W}/\text{mm}^2$ . Transmission is most efficient in direct line-of-sight to the receiver, but in practice the system can operate without interruption across a wide range of environments that include opaque enclosures or 3D features based on indirect IR reflections.

Receivers positioned in the center of the experimental arena ( $30 \times 20 \text{ cm}$ ) at a height of  $12 \text{ cm}$  indicated by red circles in Fig. 1C, each provide direct line-of-sight to the implanted device for common types of behavior studies such as operant conditioning chamber (15), open field (16), light dark assay (17), elevated plus-maze (18), place preference cage (19), water maze (20), and rodent treadmill (21). The signal is decoded using a NEC protocol in real time through an external system (ATmega328). The transmitted byte string includes fluorescent values that are time-stamped and sent via a serial universal serial bus (USB) connection for storage and analysis.

Stable operation of the  $\mu\text{C}$  relies on effective wireless power transfer, which depends strongly on the size and geometry of the receiving antenna, within the constraints set by the available subdermal space on the head of the animal. The Inset of Fig. 1C shows the architecture of two photometry device variants placed on 3D printed models of mouse skulls. The large photometry device ( $13.5 \times 10 \text{ mm}$ ;  $59 \text{ mg}$ ), applicable to large mouse strains, can support operation across large experimental arenas ( $780 \text{ cm}^2$ , at  $9\text{-W}$  RF power). The small design ( $10.5 \times 7 \text{ mm}$ ;  $45 \text{ mg}$ ) can apply to small strains and young mice in comparatively small ( $650 \text{ cm}^2$ , at  $6\text{-W}$  RF power) arenas, although extendable to larger sizes with the addition of transmission antennas. This small platform can, in fact, enable experiments in animals such as adolescent mice that are not possible with conventional optical fiber approaches (10, 14).

**Photometry Probe Design.** Fig. 1D displays an exploded-view schematic illustration of the probe. A flexible polyimide film (thickness,  $75 \mu\text{m}$ ) serves as a substrate for electrodes and interconnections formed with a patterned bilayer of Cu/Au (thickness,  $250 \text{ nm}/250 \text{ nm}$ ). The tip of the probe includes a  $\mu\text{-ILED}$  ( $270 \times 220 \times 50 \mu\text{m}$ ) and a  $\mu\text{-IPD}$  ( $300 \times 300 \times 100 \mu\text{m}$ ) placed adjacent to each other. A narrow-band optical filter ( $400 \times 400 \times 80 \mu\text{m}$ ) formed with an organic dye (ABS 473; Exciton) photolithographically defined and deposited over the  $\mu\text{-IPD}$  rejects the light from the  $\mu\text{-ILED}$  ( $468 \text{ nm}$ ) and passes light at the wavelength ( $523 \text{ nm}$ ) of fluorescence from the  $\text{Ca}^{2+}$  dye (Oregon Green 488 BAPTA-2). SI Appendix, Fig. S3 presents a series of steps for fabricating the probe.

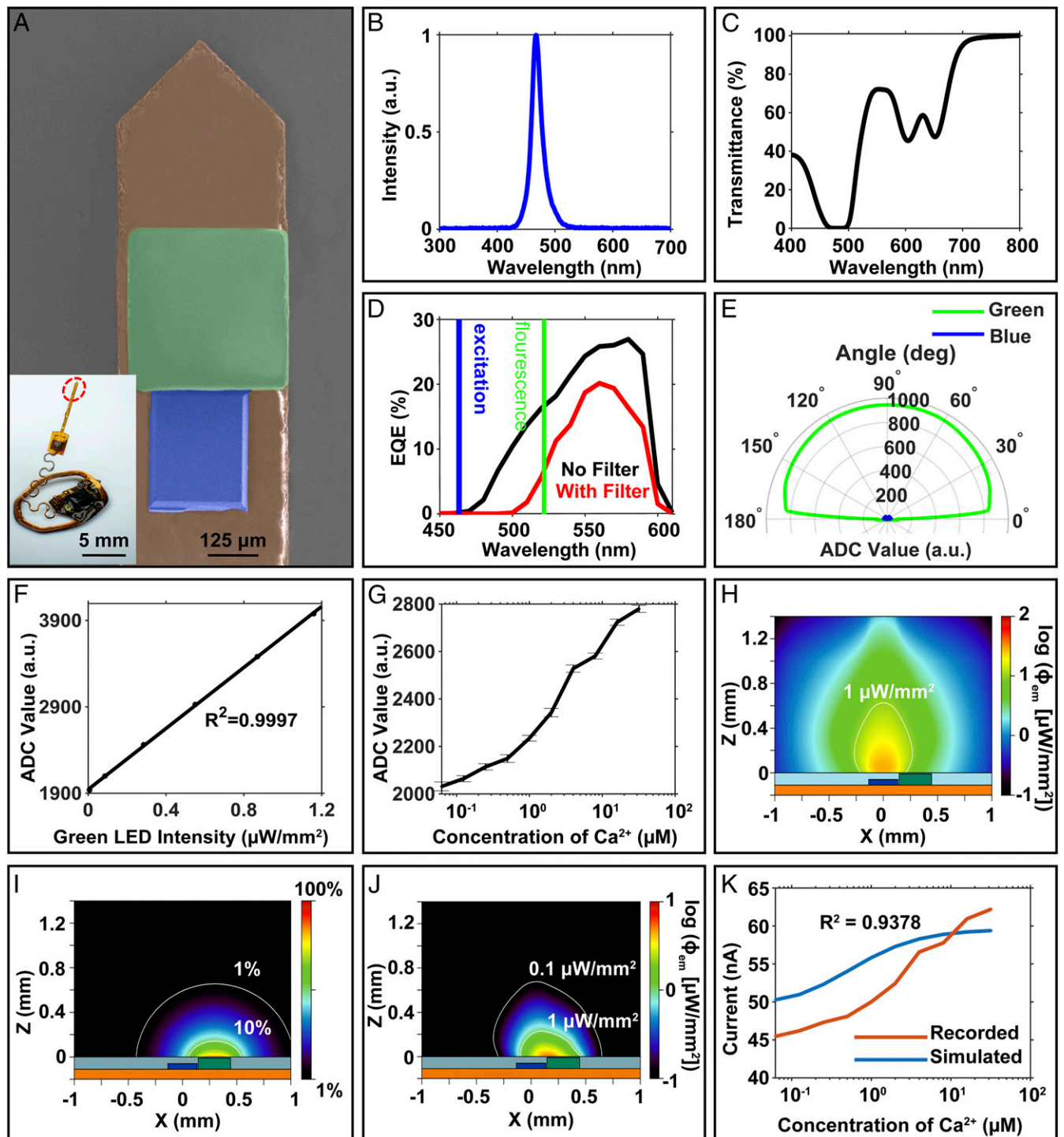
This probe connects to the main electronics body via a  $250\text{-}\mu\text{m}$ -wide serpentine structure designed to provide an effective level of stretchability that maintains strains in the metal layer that lie below the yield strain, thereby allowing for sustained elastic behavior without disrupting the electrical connectivity (22, 23) (Fig. 1E). With this arrangement, surgical placement of the probe to reach any position within the opening of the implant is possible, to target various brain regions. The probe inserts vertically into the brain, as shown in Fig. 1F. The thickest point of the electronics module, after encapsulation, is  $1,200 \mu\text{m}$  at the position of the  $\mu\text{C}$ , comparable to that of other simpler types of wireless, battery-free subdermally implantable devices (12, 14, 24).

Fig. 24 presents a colorized scanning electron microscope (SEM) image of the tip end of the photometry probe and a photograph of the integrated system. The peak emission wavelength of the  $\mu\text{-ILED}$  is  $468 \text{ nm}$  (Fig. 2B), which matches the fluorescence excitation requirement of many important GECIs, including GCaMP6 (2, 3). Characterization of the  $\mu\text{-IPD}$  under 1-sun illumination (broadband light illumination) serves as a benchmark. The  $\mu\text{-IPD}$  shows a short-circuit current ( $I_{\text{sc}}$ ) of  $2.26 \mu\text{A}$ , an open-circuit voltage ( $V_{\text{oc}}$ ) of  $1.59 \text{ V}$ , and a fill factor of  $78.5\%$  (SI Appendix, Fig. S4A). The relationship between  $I_{\text{sc}}$  and the irradiance of the input light determines important characteristics of the  $\mu\text{-IPD}$ , such as the responsivity. The  $I_{\text{sc}}$  of the  $\mu\text{-IPD}$  shows linearity with both simulated solar illumination and green light from an LED, with a responsivity of  $39.32 \mu\text{A}/\text{W}$  under white light (SI Appendix, Fig. S4B and C). The organic optical filter passes the green fluorescence signal and rejects the excitation blue light. Specifically, this filter has less than  $1\%$  transmittance for photons with wavelengths from  $465$  to  $497 \text{ nm}$  (Fig. 2C). As a result, the external quantum efficiency (EQE) of the  $\mu\text{-IPD}$  coated with this filter decreases to  $0.004\%$  at  $468 \text{ nm}$  (Fig. 2D) and moderately decreases from  $16$  to  $\sim 5\%$  at  $520 \text{ nm}$ . The result successfully minimizes the influence of the excitation light on the fluorescence signals.

The filter provides Lambertian transmission properties between  $10^\circ$  and  $170^\circ$  from the surface of the  $\mu\text{-IPD}$ . Fig. 2E illustrates the rejection characteristics, as defined by the ratio of the photoresponse to blue ( $462 \text{ nm}$ ) with respect to the green ( $520 \text{ nm}$ ) LEDs at equal irradiance ( $0.162 \mu\text{W}/\text{mm}^2$ ). The average rejection ratio at all tested angles is  $3 \pm 0.3\%$ , suitable for high-fluorescence yields in GECIs such as GCaMP6. Details are in Methods. For common in vivo instances, the fluorescence yield is  $\sim 4\%$  and  $\sim 60\%$  for  $\text{Ca}^{2+}$ -free and -saturated environments, respectively, resulting in high-contrast changes in signal from the  $\mu\text{-IPD}$  (3, 25). The wireless photometry device has a responsivity of  $0.665 \mu\text{A}/\text{W}$  to green light ( $520 \text{ nm}$ ), with a highly linear ( $R^2 = 0.9997$ ) response to irradiance at this wavelength, as shown in Fig. 2F. A fluorescent dye (Oregon Green 488 BAPTA-2;  $12.5 \mu\text{M}$ ) serves as a benchtop analog of GECIs for evaluating the fluorescence in an aqueous solution with a calcium concentration similar to that of natural intracellular calcium dynamics [typically  $0.05$  to  $0.1 \mu\text{M}$  when at rest and up to  $10 \mu\text{M}$  (26) when stimulated]. Photometric recordings of the fluorescence with this testing approach indicate the ability to detect  $\text{Ca}^{2+}$  concentrations between  $0.0625$  and  $32 \mu\text{M}$ , as shown in Fig. 2G with an average SD ( $14.24$  arbitrary units [a.u.]). Tests with the  $\mu\text{-ILED}$  disabled show a baseline dark current of  $< 22 \text{ pA}$ , which is three orders of magnitude smaller than the photocurrent at the lowest calcium concentration.

Monte Carlo simulations yield insights into the optical performance of the system. Calculations with a scattering coefficient of  $10 \text{ cm}^{-1}$  in a scenario dominated by forward scattering (dissymmetry factor of  $0.85$ ) define profiles of the  $\mu\text{-ILED}$  emission at  $470 \text{ nm}$  with an optical input power of  $0.5 \text{ mW}$ , as in SI Appendix, Fig. S5A. For a  $12.5 \mu\text{M}$  concentration of dye (Oregon Green 488 BAPTA-2), where the absorption coefficient is  $\mu_{\text{a-OG2}} = 0.38 \text{ cm}^{-1}$  at  $470 \text{ nm}$ , this emission profile results in an absorption density and a total absorbed energy with distributions shown in SI Appendix, Figs. S4C and S5B, respectively. These results characterize the amount of excitation energy involved in the generation of fluorescence. Based on the well-established relationship between fluorescence irradiance and  $\text{Ca}^{2+}$  concentration (Methods), these stimulation and absorption profiles yield corresponding fluorescent emission profiles, as shown in Fig. 2H and SI Appendix, Fig. S5D for free  $\text{Ca}^{2+}$  concentrations of  $32$  and  $0.06 \mu\text{M}$ , respectively.

The acceptance profile of the  $\mu\text{-IPD}$  with the organic filter can be simulated using Monte Carlo with a test point source that captures the role of a fluorophore with isotropic emission profile and sweeps across the entire volume above the  $\mu\text{-IPD}$ . With this



**Fig. 2.** (A) Colorized SEM image of the photometry probe (orange, polyimide; blue,  $\mu$ -ILED; green,  $\mu$ -IPD and optical filter). (B) Normalized emission spectrum of the blue  $\mu$ -ILED used for optical stimulation. (C) Transmission spectrum of an optical filter composed of layer of a photodefined epoxy (80  $\mu$ m, SU-8) doped with 1.5 wt% of an organic dye as a narrow-band absorbing filter. (D) EQE spectra of a  $\mu$ -IPD with (red) and without (black) an optical filter. The blue and green areas highlight EQEs under the maximum  $\mu$ -ILED emission (blue) and GCaMP6f fluorescence (green) wavelength regions, respectively. (E) Angular dependence of the rejection ratio of blue (462-nm) to green (520-nm) illumination displayed in ADC readings with arbitrary units (a.u.). (F) Response of the wireless photometry device to an external green light source (520 nm). (G) Fluorescence recording with SEs for solutions with different calcium concentrations (0.0625 to 32  $\mu$ M) and calcium dye (12.5  $\mu$ M; Oregon Green 488 BAPTA-2). (H) Simulated spatial distribution of fluorescence fluence at a  $\text{Ca}^{2+}$  concentration of 32  $\mu$ M and an input optical power of 0.5 mW. (I) Acceptance profile with 1% and 10% intensity contours captured by the  $\mu$ -IPD at 520 nm. (J) Fluorescence density profile captured by the  $\mu$ -IPD, obtained by the product of H and I. (K) Comparison between simulated and recorded photocurrents corrected for stray light transmission through the organic filter. The simulations assume perfect blue light rejection.

profile, no more than 50% of the emitted power reaches the  $\mu$ -IPD located at the lower hemisphere. The maximum response lies at the top surface of the  $\mu$ -IPD, as shown in Fig. 2I and without the filter in *SI Appendix, Fig. S6A*. The overall systemic response is determined by the overlap of the fluorescence profile and the  $\mu$ -IPD acceptance, as observed in Fig. 2J. Therefore, the optimum fluorescence detection volume of the photometry probe corresponds to the region between  $\mu$ -ILED and  $\mu$ -IPD. In the fluorescence conversion and detection process, the illumination volume produced by the  $\mu$ -ILED remains constant, but the fluctuations in the concentration of  $\text{Ca}^{2+}$  result in different fluorescence powers emitted by the molecular dyes (or GECIs in biological system) (for example, see Fig. 2H and *SI Appendix, Fig. S5D*). The photocurrent response measured by the  $\mu$ -IPD corresponds to the fraction of the emitted fluorescence power that reaches the photodetector's area. Fig. 2K shows the simulated photocurrents in aqueous solution compared to experimental photocurrents at different  $\text{Ca}^{2+}$  concentrations (*SI Appendix, Fig. S6B* shows same result but assuming perfect rejection of the blue light). The correlation with experimental results is excellent ( $R^2 = 0.9378$ ; Fig. 2K). The current offset ( $\sim 45$  nA in the absence of  $\text{Ca}^{2+}$ ) observed in the experimental measurements is the result of several factors: 1) the blue light rejection ratio associated with the filter is not zero ( $\sim 3\%$ ); 2) the illumination bandwidth ( $\sim 50$  nm) provides finite spectral overlap with the edge of the spectral response of the filter; and 3) blue light that travels directly from the side walls of the  $\mu$ -ILED to the  $\mu$ -IPD, which contributes to the offset photocurrent. From Monte Carlo simulations of the illumination profile, this photocurrent baseline can be estimated. The combined effects 1) and 2) produce 11.29 nA of baseline current; the effect of 3) produces 37.65 nA. As a result, the total baseline is  $\sim 49$  nA, comparable to that observed in experiment (45 nA).

**Wireless Power and Mechanical Properties.** Optimizing the power-harvesting component of the system is an important goal in engineering design. The following presents configurations for two different harvesting antennas, with dimensions and layouts configured to match the sizes of different animals and arenas.

Fig. 3A shows a small device that allows implantation on the space provided by the skull of an adolescent mouse (10.5  $\times$  7 mm). The size is 170% smaller than previously published examples of wireless battery-free optoelectronic systems designed for other purposes (1  $\text{cm}^2$ ) (12), enabled by a dual-layer antenna design optimized to deliver output power in a usable voltage regime, thereby increasing efficiency of the rectification and voltage regulation system. Fig. 3B shows harvesting characteristics with increasing load in the center of a mouse 18  $\times$  12-cm arena with a dual-loop primary antenna supplied with 3 W of RF power. Here, the minimum harvested power in this setup (17.64 mW, 8.75 V) occurs in the center of the arena, as in *SI Appendix, Fig. S7A*. The receiving antenna features a dual-sided copper coil with 7 turns, 100- $\mu\text{m}$ -wide traces with spacings of 50  $\mu\text{m}$ , for a Q factor of 23.05 (*SI Appendix, Fig. S7B*). Results of additional tests across a 28  $\times$  28-cm arena with 10 W through the primary antenna appear in Fig. 3C, at two physiologically relevant heights, i.e., 3 cm, which corresponds to the height of the head of the mouse during walking/running, and 6 cm, which represents the height in the rearing position. The 18  $\times$  12-cm and a 25.5  $\times$  25.5-cm arena tested at 5 W show similar spatial variations at heights of 3 and 6 cm, as in *SI Appendix, Fig. S7 C and D*.

Identical tests use a photometry device with comparatively large dimensions, shown in Fig. 3D, to exploit the area available on the skull of a fully grown adult mouse. The layout of the copper harvesting antenna in this case consists of 6 turns, 100- $\mu\text{m}$  trace width with 50- $\mu\text{m}$  spacing, for a Q factor of 20.46 (*SI Appendix, Fig. S7E*). Fig. 3E shows the harvesting characteristics tested in a 18  $\times$  12-cm arena, using setups similar to those

described above, at an RF power of 3 W under increasing resistive loads. This large antenna yields increased harvested power, as shown in the center of the 18  $\times$  12-cm arena in *SI Appendix, Fig. S7A* (21.68 mW, 9.43 V). This system allows improved operation in large arenas, as shown in Fig. 3F, where the power-harvesting capabilities follow similar spatial distributions as those of the small device, but with increased overall output. Further evaluations in the 18  $\times$  12-cm and a 25.5  $\times$  25.5-cm arena at an RF power of 5 W show similar spatial variations at heights of 3 and 6 cm in *SI Appendix, Fig. S7 F and G*.

Previously reported systems (25  $\times$  15-cm arena, 4-W RF power) harvest 12 mW (12), corresponding to a harvesting capability (normalized by device size) of 12  $\text{mW}/\text{cm}^2$ . The small device (0.57  $\text{cm}^2$ ) harvests 24.15 mW with the same arena and conditions (25  $\times$  15 cm, 4-W RF power), resulting in a harvesting capability of 42.37  $\text{mW}/\text{cm}^2$ , an improvement of a factor of 3.5 that follows mainly from an improved Q factor, as shown in *SI Appendix, Fig. S7 B and E*.

Power consumption characteristics appear in Fig. 3G at a system voltage of 3.3 V. The behavior follows three distinct phases, i.e., system sleep, fluorescence sampling, and data communication, marked in yellow, blue, and red, respectively. The peak power consumption is 10.37 mW during fluorescence recording. The sleep mode consumes as little as 119  $\mu\text{W}$ , thereby providing an effective means to reduce power consumption by reducing the sampling rate (*SI Appendix, Fig. S7H*).

Electrical stability in the test arena and mechanical robustness of the electrical circuitry are critical in successful operation during chronic implantation in small animals. Reducing the power consumption and increasing the harvesting capabilities enhance the stability of operation during vertical misalignments that can occur during behaviors such as rearing and sleeping. A relevant metric, which we refer to as the safety factor, is the ratio of harvested power to the average power consumption of the device. This parameter allows for estimates of the maximum misalignment angles (27) that can be tolerated anywhere in the arena without operational interruption, using *SI Appendix, Fig. S7I*. Fig. 3H shows the harvesting capability of both devices in the center of a 25.5  $\times$  25.5-cm experimental arena typically used for a range of behavioral experiments (1, 3, 5, 14, 28). A dashed black line indicates peak power consumption of the electronics for both device sizes, with a 120% safety factor to account for reductions in harvested power due to angular misalignment ( $\sim 25^\circ$  with respect to the primary antenna). Here, seamless operation of the implant can be maintained with RF powers of 5 and 7 W, respectively. These power levels are similar to those of other wirelessly powered (13.56-MHz) devices and are well within regulations approved for operation in public spaces (29, 30). Fig. 3I shows the harvesting capabilities of both devices in a large experimental arena (28  $\times$  28 cm). Here, operation cannot be sustained by the small device in the center of the arena, thereby limiting the operation for younger and smaller mouse models to arenas smaller than 25.5  $\times$  25.5 cm. Possible solutions to extend the arena size involve tracking of the subjects with activation of the corresponding antennas powered by additional power amplifier devices (31).

Fig. 3J demonstrates operating conditions with a high safety factor (437%) for a large device in a dark room at various angles across a 18  $\times$  12-cm arena with an RF power of 7 W, for stable operation with misalignments as large as  $70^\circ$ . At insufficient power, communication loss occurs rapidly with minimal erroneous or corrupted data. As outlined in Fig. 3 C and F, harvested power can fluctuate significantly depending on position in the experimental arena. An LDO actively regulates the output voltage to 3.3 V for input voltages between 3.45 and 5.6 V. Utilizing regulators with low-dropout voltages ( $\sim 150$  mV) and with overvoltage protection using 5.6-V limiting Zener diodes, the device maintains stable ADC

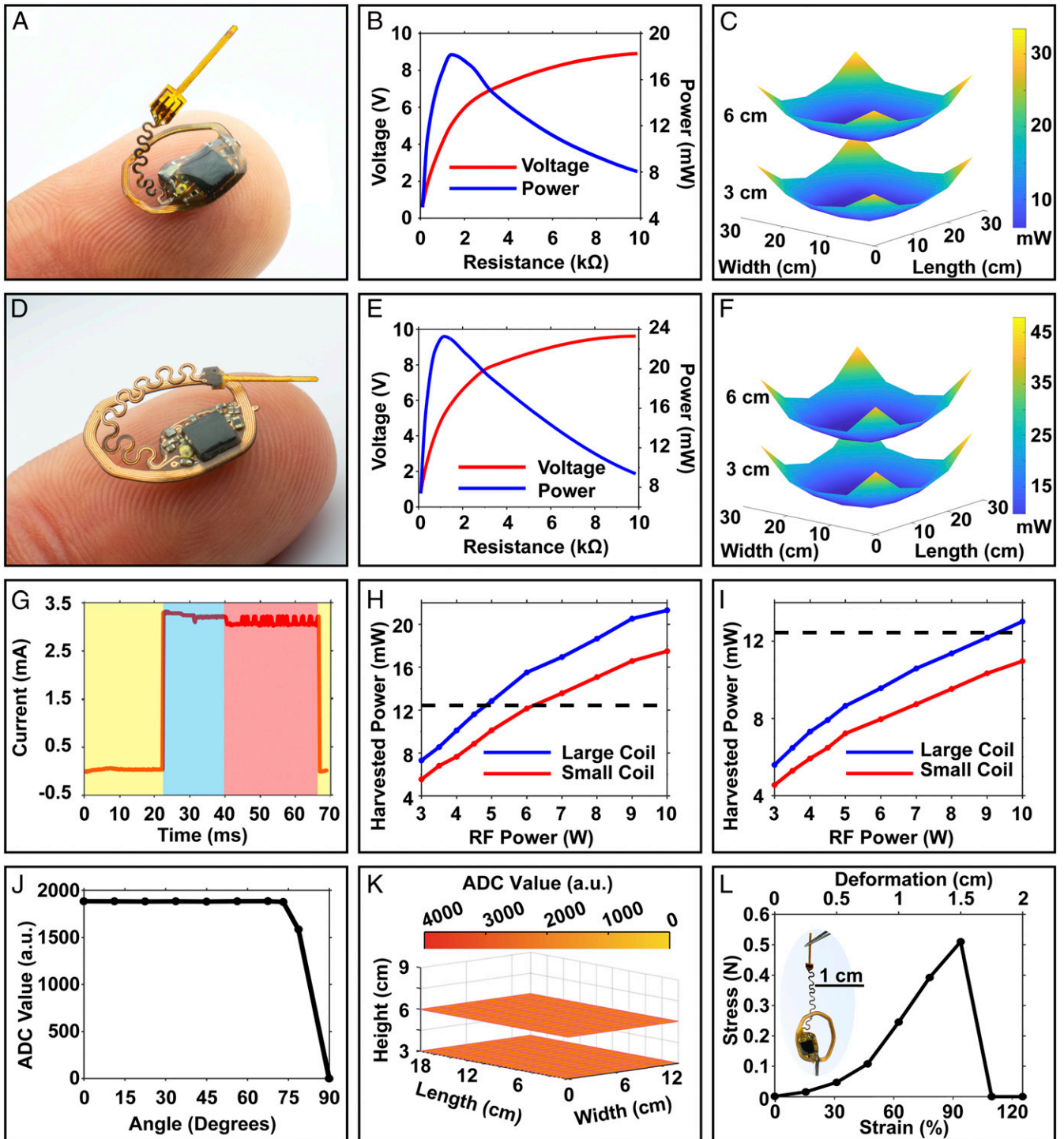


**Fig. 3.** (A–C) Highly miniaturized photometry device for implantation in small and young mice: (A) photograph of the device balancing on a finger. (B) Corresponding power vs. load curve in the center of an  $18 \times 12$ -cm arena with RF input power of 3 W. (C) Spatially resolved energy-harvesting capability of the miniaturized device with a two-turn primary antenna around an arena with dimensions of  $28 \times 28$  cm and 5-W RF input. (D–F) Large photometry device for implantation in large adult mice: (D) photograph of the device balancing on a finger. (E) Corresponding power vs. load curve in the center of an  $18 \times 12$ -cm arena with RF input power of 3 W. (F) Spatially resolved energy-harvesting capability of the large device with a two-turn primary antenna around an arena with dimensions of  $28 \times 28$  cm and 5-W RF input. (G) Time-resolved current consumption of the device during sleep (yellow), stimulation/recording (blue), and IR communication (red). (H) Harvesting performance of small and large devices in a  $25.5 \times 25.5$ -cm arena as a function of RF power input. (I) Harvesting performance of both devices in a  $28 \times 28$ -cm arena as a function of RF power input. (J) Angle-dependent ADC reading displayed in arbitrary units (a.u.) in the  $18 \times 12$ -cm arena at an input power of 6 W. (K) Height-dependent ADC reading in the  $18 \times 12$ -cm arena at an RF input power of 6 W. (L) Stress–strain curve of the serpentine interconnects.

recordings with controlled illumination at all locations in the  $18 \times 12$ -cm arena shown in Fig. 3K.

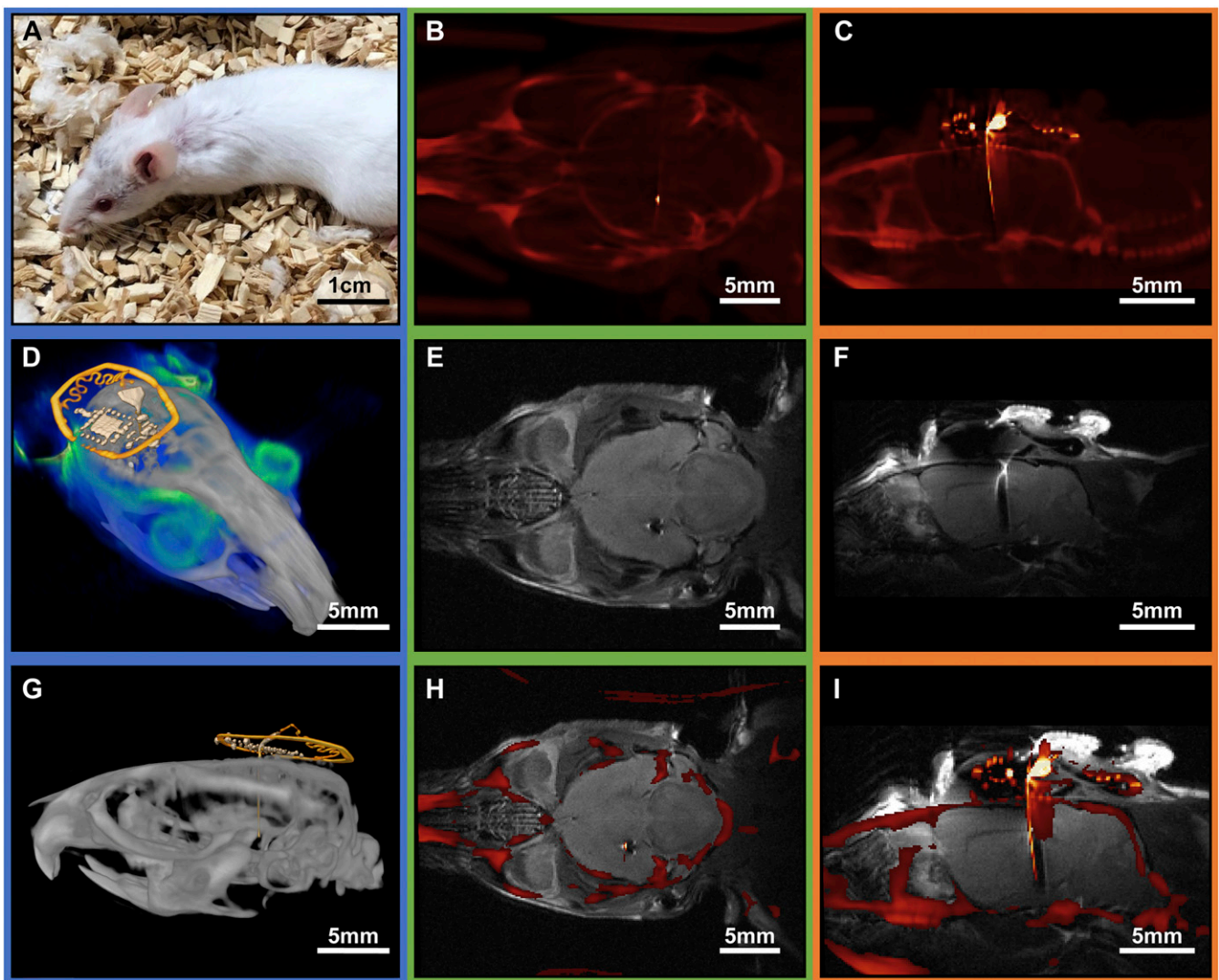
Mechanical robustness, biocompatibility, and flexible form factor are additional important considerations for successful deployment of the electrical circuitry from bending deformations exploits a potting process with a UV curable adhesive that has a low level of shrinkage from the curing process (32). Further encapsulation with polyurethane (PU) (33) and a coating of polydimethylsiloxane (PDMS) ( $\sim 10 \mu\text{m}$  thick) provides a biocompatible barrier to biofluids (34) and a degree of modulus matching with surrounding tissues (10) that reduces damage to these tissues.

Fig. 3L shows the electromechanical characteristics of the injectable probe when stretched relative to the electronics platform. Here, a high tolerance to strain allows for elongations of up to 1.5 cm in comparison to the relaxed state, corresponding to a tensile strain of 93.75% without disruption of electrical function.

This elongation allows the probe to be bent out of plane and to be placed within the opening of the device to reach the desired brain region.

**Device Implantation and Imaging.** The thin geometry, small dimension, and lightweight nature of the device minimize loads on the animal and allow for seamless recovery shortly after implantation. Fig. 4A shows an animal 20 d postsurgery with skin and fur completely recovered. Elimination of the supercapacitor featured in previously published examples (12) decreases the size and bulk of the device, and removes all magnetic components. The result is a device that is compatible with both MRI and  $\mu\text{CT}$  imaging. Standard imaging procedures yield very little distortions, comparable to those of recently reported optogenetic stimulators that have significantly reduced electronic complexity (11).

Fig. 4B and C show  $\mu\text{CT}$  images of the electronics and photometry probe and their position with respect to bone structure. This imaging capability is especially valuable for rapid postsurgery



**Fig. 4.** (A) Photograph of a mouse 20 d after implantation of a small photometry device. (B) Transverse CT reconstruction of the implanted device. (C) Sagittal CT reconstruction of a slice that illustrates the position of the implant. (D) Three-dimensional rendering that combines MRI (blue) and CT (gray and yellow marked device structures) results. (E) Transverse MRI reconstruction of the device illustrating imaging capability around the target area. (F) Sagittal MRI reconstruction of the device illustrating minimal distortion of the brain. (G) Postprocessed sagittal CT scan with false color device structures (yellow). (H) Transverse MRI and CT overlay of the device, indicating successful registration and low-dimensional image distortion in both MRI and CT. (I) Coregistered sagittal MRI and CT overlay.

analysis to validate implant targeting. Tissue contrast of the MRI images (Fig. 4 D–F) shows no distortion in the target area. The results can be used to identify brain regions on a per-animal basis,

to eliminate effects of natural animal-to-animal variances and variability in surgical procedures. High-dimensional accuracy can be seen in coregistered MRI and  $\mu$ CT images (Fig. 4 D and G–I).

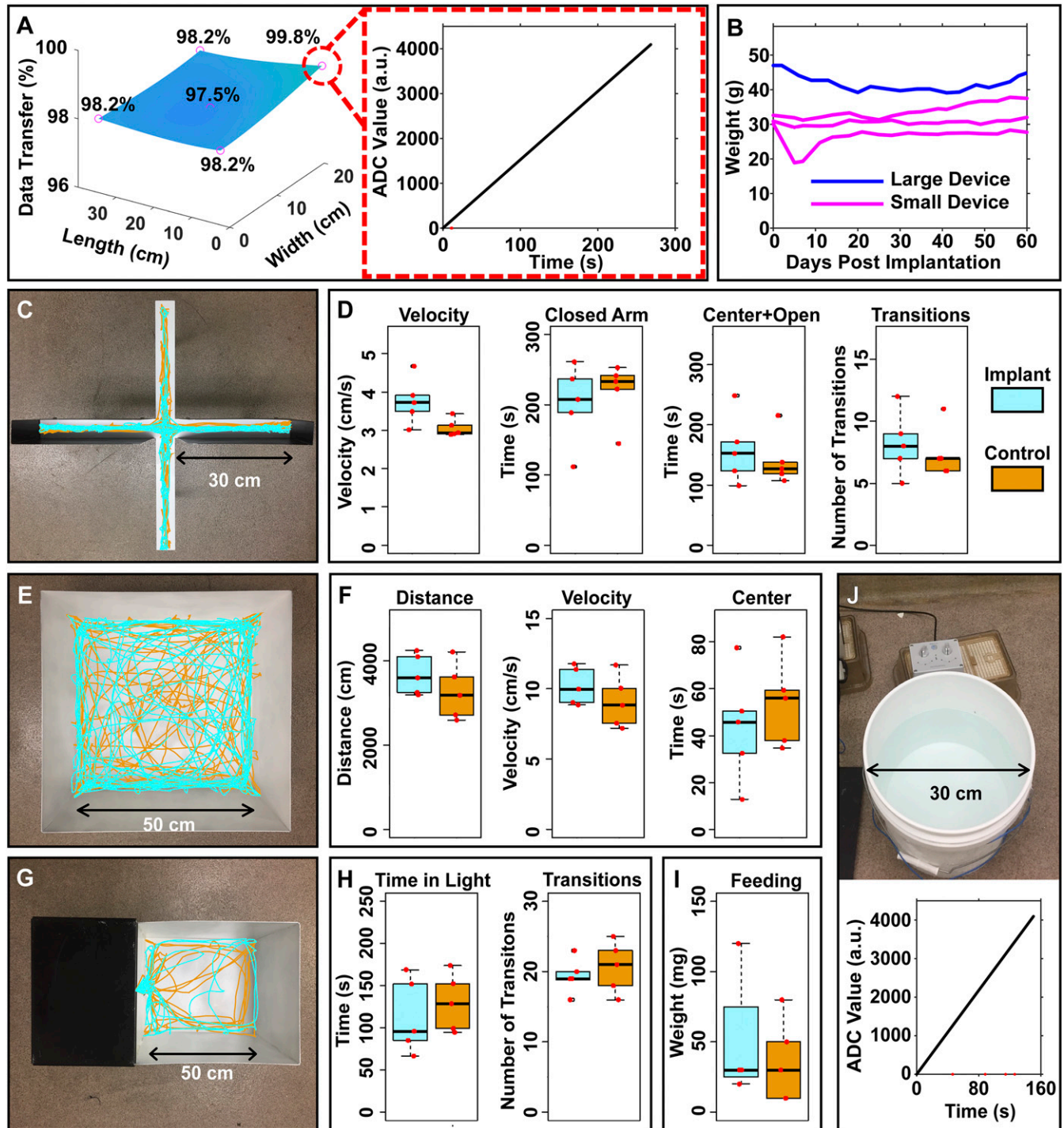


**Fig. 5.** (A) Data transfer rates for a freely behaving subject (Left) in a test pattern designed to evaluate performance (Right) (dropped data points marked in red). (B) Weight of animal as a function of time after implantation. (C) Elevated plus-maze experiment with overlay of traces of motion of both implanted and control mice. (D) Average velocity, time in the closed arm, time in the center and open arms, and number of transitions between closed and open arms of the mice in the elevated plus-maze. (E) Open-field experiment with overlay of traces of motion of both implanted and control mice. (F) Distance traveled, average velocity, and time spent in the center of the arena for mice in an open-field assay. (G) Light-dark room experiment with overlay of traces of motion of both implanted and nonimplanted mice. (H) Time spent in the light room and number of transitions between the light and dark room of both implanted and control mice in a light-dark assay. (I) Weight of the pellet consumed during a 1-h feeding session. (J) Digital data collection displayed in ADC readings with arbitrary units (a.u.) of a mouse during a forced-swim test in a 5-gallon cylindrical tank with data packets dropped shown in red.



**Postimplantation Recording and Behavioral Impact.** Experiments that exploit the electronic and mechanical features of these devices in live animal models demonstrate successful and reliable operation across a home cage (30 × 20 cm) with 8-W RF input (safety factor, 137%), as evident by low loss of packets (Fig. 5A) each containing 12-bit integers. Here, evaluations of sampling capability use a test program that transmits incremental values to validate the IR communication link, as shown in the *Inset* of Fig. 5A. A set of experiments that tracks the position of the animal throughout the arena and records packet loss as a function of position reveals that only eight data packets drop during a typical 4.5-min test data segment. This level of performance is comparable to other low-power wireless communication methods, including Bluetooth (35). Additional tests probe various locations of implanted mice in an arena (30 × 20 cm) with recording times of ~23 min. In a benchtop endurance test, with the device located in the center of a home cage at 5 W of RF power, experimental results in *SI Appendix, Fig. S8* demonstrate continuous recording of an external green light source (0.38 mW/mm<sup>2</sup>, 520 nm) pulsing at 1-s intervals for 24 h in a dark room with 0 packet loss and no change in signal magnitude or timing.

This high level of robustness in data communication follows from a sensitivity in the receiver (0.15 mW/m<sup>2</sup>) and a wide field of view of 90° (*SI Appendix, Fig. S9 A and B*) for recording both line-of-sight and indirect signals. Smaller arenas can be recorded with a single receiver, while larger arenas benefit from multi-receiver setups, as depicted in *SI Appendix, Fig. S8B*, where five receivers connected in parallel improve the detectivity.

Both large and small devices show no loss in performance for at least 2 months after implantation. Mice after surgery show recovery speeds comparable to other wireless and optically tethered photometry systems (10, 36, 37), as shown in Fig. 5B, with unrecovered mice in *SI Appendix, Fig. S10*. Animal welfare is also not affected by either the surgery or the presence of the device, as indicated by the steady weight progression of the animals postsurgery.

As mentioned previously, the small photometry device (10.5 × 7 mm; 45 mg) can record neural dynamics in young mice (10 to 11 wk). Tests of behavioral impacts on anxiety, locomotion, and feeding involve a cohort of implanted animals ( $n = 5$ ) and a control group ( $n = 5$ ). Anxiety and locomotion tests involve analysis of both movement and spatial preferences within open-field and elevated plus-maze assays (38, 39). Implanted mice automatically tracked in the elevated plus-maze indicate no visible difference in anxiety or locomotion. Representative traces of an implanted and control subject are in Fig. 5C. Analysis of the cohort with unpaired  $t$  tests between average velocity ( $P = 0.060$ ), time spent in the closed arms ( $P = 0.595$ ), time spent in both center and open arms ( $P = 0.595$ ), and number of closed and open arm transitions ( $P = 0.605$ ) reveals no significant difference between the two groups, as summarized in Fig. 5D. The open-field experimental paradigm with implanted and control animals also reveals similar behavioral patterns (Fig. 5E). Analysis of the cohort shows no increased levels of anxiety or impairment in locomotion. Furthermore, results displayed in Fig. 5F with implanted mice show no significant differences in total distance traveled ( $P = 0.298$ ), average velocity ( $P = 0.299$ ), or total time spent in the center of the arena ( $P = 0.477$ ). Light-dark box experiments for analyzing anxiety compare the drive between exploration and aversion to open and brightly lit areas (40). Movement traces of representative animals in Fig. 5G show no significant differences in behavior between subjects with implant and control. Analysis using unpaired  $t$  tests of time spent in light arena ( $P = 0.540$ ) and number of transitions between the light and dark areas ( $P = 0.563$ ) are in Fig. 5H. The result reveals minimal anxiety levels in the implanted mice and the control group. Elevated plus-maze, open-field, and light-dark box assays indicate that the implant had no significant effect on the anxiety level or locomotive behaviors. Both control and implanted mice with prior access to food placed in a test arena (29.2 × 19 × 12.7 cm) exhibit feeding behaviors (41)

that show no significant differences through an unpaired  $t$  test ( $P = 0.626$ ) in 1-h total food intake between groups, as in Fig. 5I.

The untethered operation of the system coupled with its small weight and the quick recovery of the test subjects following implantation creates possibilities for recording in behavioral paradigms that are not possible with current technologies. Measurements of freely moving mice during a forced-swim test, shown in Fig. 5J, highlights compliance with 3D environments and reveals seamless recording of neural dynamics in arenas (707 cm<sup>2</sup>) that are difficult or impossible to address with tethered techniques (10, 42). A communication experiment using five IR receivers, analogous to previously described tests in the home cage (Fig. 5A), establishes that operation in aquatic environments offers similar link quality, with only 1.5% of the data packets dropped during a recording period of ~10 min for the full duration of a forced-swim test.

**Conclusions.** In summary, this paper introduces a fully subdermally implantable photometry system that enables interrogation of calcium transients (0.0625 to 32  $\mu$ M) with a battery-free, miniaturized form factor for recordings in freely behaving subjects with low power consumption (10.37 mW). The thin, low-profile geometry facilitates subdermal implantation even in small rodent animal models such as young mice. Significant improvements in energy harvesting and in device geometry create opportunities in recording GECs in freely behaving subjects with high flexibility in probe placement for broad-ranging applications in the dissection of neural circuits. The platform is fully compatible with live imaging by MRI and  $\mu$ CT, and is constructed using manufacturing techniques adopted from the semiconductor industry. Behavioral experiments reveal that the implantation and operation of the device does not impact behavior of subjects in a variety of scenarios including aquatic settings. Collectively, these features suggest a potential for widespread utility in neuroscience research.

## Methods

**Flexible Circuit Fabrication.** Pyralux (AP8535R; constituent layers, 17.5- $\mu$ m copper, 75- $\mu$ m polyimide, and 17.5- $\mu$ m copper) served as a substrate. The copper traces, vias, and device outline were defined using a UV (355-nm) laser ablation system (LPKF; Protolaser U4) with subsequent ultrasonic cleaning (Vevor; Commercial Ultrasonic Cleaner 2L) for 10 min in flux (Superior Flux and Manufacturing Company; Superior #71) and 1 min in isopropyl alcohol (IPA) (MG Chemicals) and rinsing with deionized (DI) water to remove oxidation and organic residue. Via connections were established manually with copper wire (100  $\mu$ m) and low-temperature solder (Chip Quik; TS3911T).

**Photometry Probes.** Fabrication of the photometry probe began with spin coating a thin layer of PDMS adhesive on a glass slide. A polyimide film (75  $\mu$ m thick) served as the substrate for the probe, laminated on the PDMS adhesive. Photolithography and a lift-off process in acetone defined patterns of Cu/Au (formed by electron beam evaporation; thickness of ~500 nm) electrodes and interconnects on polyimide film. Spin coating and patterning a layer of photodefinable epoxy (SU-8 2002; Microchem) formed an insulating layer on the electrodes with selective openings for the  $\mu$ -IPD and  $\mu$ -ILED. In/Ag solder pastes (Indalloy 290; Indium Corporation) were placed on electrodes in the openings. Transfer printing delivered the electrode pads of the  $\mu$ -IPD (TCE12-589; Three Five Materials) and  $\mu$ -ILED (C460TR2227-0216; Cree) onto the pastes. A subsequent heating process at 150 °C for 1 min formed a robust mechanical and electrical connection between the  $\mu$ -IPD,  $\mu$ -ILED, and Cu/Au electrodes. A spin-coated layer of a narrow-band organic absorber (ABS 473; Exciton) mixed into a photodefinable epoxy (SU-8 2100; Microchem) (1.5 wt%) formed the optical filter on the  $\mu$ -IPD. Laser cutting defined the pattern of the injectable probe and dip coating in PDMS formed the encapsulation layer of the final device.

The pads of the photometry probes were cleaned using Kimwipes Low-Lint Wipers (34155; Kimberly-Clark Professional) with IPA. These probes were electrically joined to the flexible circuit via reflow low-temperature soldering. The connection between the probe and device was then cleaned with IPA to ensure adequate mechanical adhesion using UV curable glue (Damn Good; 20910DGL) and cured under a UV lamp (24 W, 10 min) and subsequently baked in an oven (50 °C, 20 min).

**Electrical Tuning, Components, and Coding.** Commercially available components were placed by hand and reflowed with low-temperature solder. A half-bridge rectifier was built using 2001 components (0.6 × 0.3 mm) for the tuning capacitors, smoothing capacitor, and low-capacitance, low-forward voltage Schottky diodes (Skyworks). Tuning capacitors were chosen to produce the lowest voltage standing wave ratio at 13.56 MHz during reflection testing with a reflection bridge (Siglent; SSA 3032X; RB3X20). A Zener diode (Comchip Technology Corporation; 5.6 V) provided overvoltage protection and a 3.3-V LDO stabilized the input voltage to the microcontroller. A low-power microcontroller (Atmel; ATtiny 84) controlled the timing of the activation of the  $\mu$ -LED, the readout of the  $\mu$ -IPD, and infrared communication. The microcontroller software was programmed using a Tiny AVR Programmer with a USB interface before mounting on the flexible circuit. The blue  $\mu$ -LED current was set using a 1-k $\Omega$  resistor to control irradiance of the blue LED stimulations. An amplifier (Analog Devices; ADA4505-1) was used in a transimpedance configuration to convert the current output of the  $\mu$ -IPD into a voltage, which was then digitized. The digital signal was modulated (57 kHz) and transmitted using a current limited IR LED with a 0402 package (1.0 × 0.5 mm).

**Encapsulation.** Devices were rinsed with IPA to remove any particulates. Components were fixed to the flexible circuit using UV-curable glue (Damm Good; 20910DGFL) subsequently cured under a UV lamp (24 W, 10 min) and cross-linked in an oven (80 °C, 20 min) to ensure adhesion of additional layers. Devices were then encapsulated via spray coating of PU (MG Chemicals; Premium Polyurethane Conformal Coating) and cured in an oven (80 °C, 1 h), followed by a second coating and oven cure (80 °C, 24 h). The devices were finally encapsulated with PDMS through dip coating and curing at 80 °C for 24 h.

**Device Electrical Characteristic Testing.** Voltage and power-harvesting characteristics of the device in the center of an 18 × 12-cm arena powered with an RF power of 3 W were determined using a shunt resistor with voltage measurement (Aneng; AN8008). A shunt resistor (1.5 k $\Omega$ ) was chosen to impedance match with the rectifier. Peak power measurements of location-dependent harvesting capabilities with dual-loop antennas with dimensions of 18 × 12, 25.5 × 25.5, and 28 × 28 cm result in voltage readings that were used to calculate power output of the implants. Harvesting capabilities were tested at heights of 3 and 6 cm. The primary antenna was powered with RF input of 3 and 10 W, and testing was performed in the center of the three arena designs. Measurements of stable operation were conducted at two heights in an 18 × 12-cm arena in a dark condition with an RF power of 4 W while collecting IR data using a single receiver located 20 cm above the arena surface. Current consumption of the device was recorded using a laboratory power supply (5 V) and a current meter (LowPowerLab; CurrentRanger) with an internal shunt of 10  $\Omega$  and cascaded amplifiers (Maxim Integrated; MAX4239) with acquisition of real-time current consumption via an oscilloscope (Siglent; SDS 1202X-E). The angular dependence of the power-harvesting capability was tested by varying the angle of the implants with respect to the arena floor from 0 to 90° using a rotational jig while monitoring ADC recordings in a dark room using the digital communication IR receiver (Vishay Semiconductors; TSDP34156).

**Device Strain–Stress Testing.** The device was mounted to a scale (Mettler Toledo; AB104-S) with both ends of the serpentine connected to a multimeter to measure electrical continuity. The probe connection side of the serpentine was then fixed to a fixture to adjust strain of the device. The serpentine structure was adjusted to its base length and stress was recorded after stretching the device at 2.5-mm increments.

**Functional Ex Vivo Testing.** Angle-dependent rejection ratios of blue and green light through the thin film optical filter were tested by using green (520 nm) and blue (462 nm) LEDs directed at multiple angles (10° to 170°) on the  $\mu$ -IPD at the same irradiance (0.162  $\mu$ W/mm<sup>2</sup>). The rejection ratio was then calculated as the average ratio of the irradiance measured at the  $\mu$ -IPD. The photoresponsive characteristics of the  $\mu$ -IPD were tested using a green LED (520 nm) with intensity controlled by a constant voltage power supply (RIDEN; DPS3005) and calibrated by a spectral power meter (Thorlabs; PM100). In both tests, the photocurrent of the  $\mu$ -IPD was preprocessed in the  $\mu$ C (amplification and digitalization) and transmitted wirelessly.

A stock solution of 64  $\mu$ M calcium chloride (Sigma-Aldrich) in DI water was prepared and used to produce twofold serial dilutions ranging from 0.0625 to 32  $\mu$ M with a final volume of 0.24 mL. A 3 mM stock solution of Oregon Green (488 BAPTA-2; Thermo Fisher Scientific) in anhydrous dimethyl sulfoxide was mixed with each calcium solution to produce 12.5  $\mu$ M concentration of

dye across each vial. The solutions of dye and calcium were lightly vortexed in a vial to ensure adequate mixing prior to data acquisition. The photometry device was powered using a dual-loop antenna encircling an 18 × 12-cm arena and powered with RF at 3 W in a dark room to prevent optical noise. The photometry probe was inserted into each test solution and readouts were recorded. After each test, the probe was removed from the solution and lightly rinsed of excess solution using DI water before recording the next set of data.

**Fluorescence and Photocurrent Numerical Calculations.** Detailed information on fluorescence and photocurrent numerical calculation methods is available in *SI Appendix, Text ST.1*.

**Surgical Procedure.** All procedures were approved under Northwestern University and The University of Arizona Institutional Animal Care and Use Committee. Seven- to 8-wk-old CD1 mice or C57BL/6 (Charles River) were acclimated at least for 48 h and were implanted with the photometry device using a stereotaxic device. The animals were checked daily for moribund or distress condition.

The devices were implanted in the left hemisphere of 7- to 8-wk-old CD1 mice at –3.0 mm anteroposterior (AP), +2.0 mm mediolateral (ML), +6.9 mm dorsoventral (DV) from bregma or C57BL/6 (Charles River) at –1.0 mm AP, +1.0 mm ML, +6.9 mm DV from bregma with at least 48 h of acclimation before surgery. Mice were administered anesthesia using 2 to 3.5% isoflurane. The stereotaxic frame and components were sprayed and wiped down with 70% ethanol and placed on a fresh laboratory mat. A fresh paper towel was placed in the platform for each new animal. All surgical instruments were autoclaved at the start of the day. Surgeons wore clean laboratory coats, used sterile gloves and masks, and changed gloves for each animal. The animal's head fur was shaved, and the site scrubbed with Betadine and rinsed with 70% ethanol. The animal was then mounted in the stereotaxic frame using ear bars and an incisor clamp. The animal's eyes were treated with an eye lubricant gel to prevent drying. A 10-mm incision was made with a #10 blade from behind the eyes to the ears and down to the cranium. The scalp was gently spread apart, and the underlying fascia retracted on both sides with Halstead Mosquito forceps. The site was rinsed with fresh saline and swabbed dry. The bregma was used as the stereotaxic zero. A 27-gauge needle was stereotactically placed 2.5 mm to the right of midline on the coronal suture, and this site marked with an autoclaved #2 pencil. A small bur hole was made with a variable speed Dremel power tool with a 1.0-mm bur. The probe was inserted into the bur hole with the base of the device fixed to the surface of the skull using super glue. The incision was closed with 4.0 nonabsorbable sutures; the animal was allowed to recover for 5 to 10 min before transfer back to the cage area facility. Mice recovered for days before testing for data transmission rates.

**$\mu$ CT Imaging and MRI.** Detailed information on  $\mu$ CT imaging and MRI parameters are available in *SI Appendix, Text ST2*.

**Behavioral Experiments.** Both control mice ( $n = 5$ ) and mice ( $n = 5$ ) at 1 wk postimplantation received a minimum of 15 min of habituation to the testing room and experimenters a day before anxiety behavioral experiments. Anxiety experiments were conducted in an open-field test (50 × 50 × 30 cm, a 25 × 25-cm square center was defined as “center” in analysis), elevated plus-maze (40 cm above the floor) with two opposing open arms (30 × 5 × 15 cm) and two opposing closed arms (30 × 5 × 15 cm), and light–dark box (20 × 50 × 30 cm; dark box, 20 × 20 × 30 cm) each for 6 min per mouse with the arena cleaned with 70% isopropyl in-between each test. Mice were recorded with a Logitech webcam and analyzed using Ethovision (XT 10.0; Noldus Information Technology) to track mouse position. During light–dark box experiment, mouse position was tracked only in the light box. Feeding experiments were conducted simultaneously, with each pellet weighed before the 1-h feeding session. Each arena (29.2 × 19 × 12.7 cm) was cleaned before starting the experiment to minimize urine from affecting the weight of the pellet and feeding behavior of the mice. Each pellet was inspected for urine and weighted again along with any crumbs from the arena. Data from one mouse was rejected due to urine on the food. Forced-swim tests of implanted mice were conducted in a 5-gallon bucket (diameter, 30 cm) that was cleaned and filled with water. A dual-loop antenna with a diameter of 30 cm around the cylindrical container with 1-cm separation at the height of the water level were used to wirelessly power the device at 8-W RF power. Data uplink was established with five parallel IR receivers placed 15 cm above the water level. The data communication link was recorded during ~10 min of full forced-swim tests.

**Code and Materials Availability.** All data needed to support the conclusions presented in this paper are available in the manuscript and/or [SI Appendix](#).

**ACKNOWLEDGMENTS.** We acknowledge funding support from National Institute of Biomedical Imaging and Bioengineering–NIH Training Grant

T32EB000809 for Biomedical Imaging and Spectroscopy (A.B.); National Heart, Lung, and Blood Institute–NIH Grant 5T32HL007955-19 (J.A.R.); George Washington University Department of Biomedical Engineering startup funds (L.L.); and The University of Arizona Department of Biomedical Engineering startup funds (P.G.). We thank Anil Brikha for preparations of CT and MRI 3D renderings.

1. J. Akerboom *et al.*, Optimization of a GCaMP calcium indicator for neural activity imaging. *J. Neurosci.* **32**, 13819–13840 (2012).
2. Y. Zhao *et al.*, An expanded palette of genetically encoded Ca<sup>2+</sup> indicators. *Science* **333**, 1888–1891 (2011).
3. T.-W. Chen *et al.*, Ultrasensitive fluorescent proteins for imaging neuronal activity. *Nature* **499**, 295–300 (2013).
4. L. A. Gunaydin *et al.*, Natural neural projection dynamics underlying social behavior. *Cell* **157**, 1535–1551 (2014).
5. G. Cui *et al.*, Concurrent activation of striatal direct and indirect pathways during action initiation. *Nature* **494**, 238–242 (2013).
6. A. L. Falkner, L. Grosenick, T. J. Davidson, K. Deisseroth, D. Lin, Hypothalamic control of male aggression-seeking behavior. *Nat. Neurosci.* **19**, 596–604 (2016).
7. C. Armstrong, E. Krook-Magnuson, M. Oijala, I. Soltesz, Closed-loop optogenetic intervention in mice. *Nat. Protoc.* **8**, 1475–1493 (2013).
8. A. Gilletti, J. Muthuswamy, Brain micromotion around implants in the rodent somatosensory cortex. *J. Neural Eng.* **3**, 189–195 (2006).
9. A. Sridharan, S. D. Rajan, J. Muthuswamy, Long-term changes in the material properties of brain tissue at the implant-tissue interface. *J. Neural Eng.* **10**, 066001 (2013).
10. L. Lu *et al.*, Wireless optoelectronic photometers for monitoring neuronal dynamics in the deep brain. *Proc. Natl. Acad. Sci. U.S.A.* **115**, E1374–E1383 (2018).
11. P. Gutruf *et al.*, Fully implantable optoelectronic systems for battery-free, multimodal operation in neuroscience research. *Nat. Electron.* **1**, 652–660 (2018).
12. H. Zhang *et al.*, Wireless, battery-free optoelectronic systems as subdermal implants for local tissue oximetry. *Sci. Adv.* **5**, eaaw0873 (2019).
13. J. Kim *et al.*, Miniaturized flexible electronic systems with wireless power and near-field communication capabilities. *Adv. Funct. Mater.* **25**, 4761–4767 (2015).
14. G. Shin *et al.*, Flexible near-field wireless optoelectronics as subdermal implants for broad applications in optogenetics. *Neuron* **93**, 509–521.e3 (2017).
15. J. Duran *et al.*, Lack of neuronal glycogen impairs memory formation and learning-dependent synaptic plasticity in mice. *Front. Cell. Neurosci.* **13**, 374 (2019).
16. V. Carola, F. D'Olimpio, E. Brunamonti, F. Mangia, P. Renzi, Evaluation of the elevated plus-maze and open-field tests for the assessment of anxiety-related behaviour in inbred mice. *Behav. Brain Res.* **134**, 49–57 (2002).
17. J. A. Bouwknecht, R. Paylor, Behavioral and physiological mouse assays for anxiety: A survey in nine mouse strains. *Behav. Brain Res.* **136**, 489–501 (2002).
18. R. J. Rodgers, A. Dalvi, Anxiety, defence and the elevated plus-maze. *Neurosci. Biobehav. Rev.* **21**, 801–810 (1997).
19. C. L. Cunningham, C. M. Gremel, P. A. Groblewski, Drug-induced conditioned place preference and aversion in mice. *Nat. Protoc.* **1**, 1662–1670 (2006).
20. C. D. Barnhart, D. Yang, P. J. Lein, Using the Morris water maze to assess spatial learning and memory in weanling mice. *PLoS One* **10**, e0124521 (2015).
21. M. S. Costa *et al.*, Treadmill running frequency on anxiety and hippocampal adenosine receptors density in adult and middle-aged rats. *Prog. Neuropsychopharmacol. Biol. Psychiatry* **36**, 198–204 (2012).
22. Y.-Y. Hsu *et al.*, Design for reliability of multi-layer stretchable interconnects. *J. Microelectromech. Syst.* **24**, 95014 (2014).
23. B. Plovie, F. Bossuyt, J. Vanfleteren, Stretchability—the metric for stretchable electrical interconnects. *Micromachines (Basel)* **9**, 382 (2018).
24. D. M. Russell, D. McCormick, A. J. Taberner, S. C. Malpas, D. M. Budgett, A high bandwidth fully implantable mouse telemetry system for chronic ECG measurement. *Annu. Int. Conf. IEEE Eng. Med. Biol. Soc.* **2011**, 7666–7669 (2011).
25. L. M. Barnett, T. E. Hughes, M. Drobizhev, Deciphering the molecular mechanism responsible for GCaMP6m's Ca<sup>2+</sup>-dependent change in fluorescence. *PLoS One* **12**, e0170934 (2017).
26. C. Grienberger, A. Konnerth, Imaging calcium in neurons. *Neuron* **73**, 862–885 (2012).
27. B. W. Flynn, K. Fotopoulou, Rectifying loose coils: Wireless power transfer in loosely coupled inductive links with lateral and angular misalignment. *IEEE Microw. Mag.* **14**, 48–54 (2013).
28. W. Zong *et al.*, Fast high-resolution miniature two-photon microscopy for brain imaging in freely behaving mice. *Nat. Methods* **14**, 713–719 (2017).
29. IEEE Standards Coordinating Committee 28, *IEEE Standard for Safety Levels with Respect to Human Exposure to Radio Frequency Electromagnetic Fields, 3 kHz to 300 GHz* (Institute of Electrical and Electronics Engineers, 1992).
30. P. Gutruf, J. A. Rogers, Implantable, wireless device platforms for neuroscience research. *Curr. Opin. Neurobiol.* **50**, 42–49 (2018).
31. S. I. Park *et al.*, Stretchable multichannel antennas in soft wireless optoelectronic implants for optogenetics. *Proc. Natl. Acad. Sci. U.S.A.* **113**, E8169–E8177 (2016).
32. P. Swanson, Advances in light curing adhesives and coatings lead to process and quality benefits in electronics manufacturing. *Proceedings of the Technical Program: NEPCON West '97* (Reed Exhibition Companies, 1997), pp. 929–942.
33. Z. Ren, G. Chen, Z. Wei, L. Sang, M. Qi, Hemocompatibility evaluation of polyurethane film with surface-grafted poly(ethylene glycol) and carboxymethyl-chitosan. *J. Appl. Polym. Sci.* **127**, 308–315 (2013).
34. Y. Chen, Y.-S. Kim, B. W. Tillman, W.-H. Yeo, Y. Chun, Advances in materials for recent low-profile implantable bioelectronics. *Materials (Basel)* **11**, 522 (2018).
35. E. Tsimbalo *et al.*, “Mitigating packet loss in connectionless Bluetooth Low Energy” in *2015 IEEE 2nd World Forum on Internet of Things (WF-IoT)* (IEEE, 2015), pp. 291–296.
36. Y. Sych, M. Chernysheva, L. T. Sumanovski, F. Helmchen, High-density multi-fiber photometry for studying large-scale brain circuit dynamics. *Nat. Methods* **16**, 553–560 (2019).
37. L. Zhang *et al.*, Miniscope GRIN lens system for calcium imaging of neuronal activity from deep brain structures in behaving animals. *Curr. Protoc. Neurosci.* **86**, e56 (2019).
38. L. E. Gonzalez, S. E. File, A five minute experience in the elevated plus-maze alters the state of the benzodiazepine receptor in the dorsal raphe nucleus. *J. Neurosci.* **17**, 1505–1511 (1997).
39. M. L. Seibenhener, M. C. Wooten, Use of the open field maze to measure locomotor and anxiety-like behavior in mice. *J. Vis. Exp.* **96**, e52434 (2015).
40. T. Serchov, D. van Calker, K. Biber, Light/dark transition test to assess anxiety-like behavior in mice. *Bio Protoc.* **6**, e1957 (2016).
41. R. A. Essner *et al.*, AgRP neurons can increase food intake during conditions of appetite suppression and inhibit anorexigenic parabrachial neurons. *J. Neurosci.* **37**, 8678–8687 (2017).
42. O. V. Bogdanova, S. Kanekar, K. E. D'Anci, P. F. Renshaw, Factors influencing behavior in the forced swim test. *Physiol. Behav.* **118**, 227–239 (2013).